Similarity of dissipation and enstrophy in particle-induced small-scale turbulence

Zhuo Wang, Kun Luo, Junhua Tan, Dong Li, and Jianren Fan*
State Key Laboratory of Clean Energy Utilization, Zhejiang University, Hangzhou 310027, China

(Received 2 December 2018; published 6 January 2020)

Small-scale turbulence is the most promising place to establish proper turbulence theory. An understanding of the relationships between the two descriptors of small-scale turbulence, namely, enstrophy and dissipation, is one of the longstanding research topics. Meanwhile, current knowledge on this point is controversial because past observations are inconsistent with the existing theoretical arguments. We present a different approach to investigate this problem by enhancing small-scale fluctuations with finite-size particles. In this particle-augmented turbulent flow, several common observations about small-scale turbulence are obtained with recent high-Reynolds-number studies, though the operating conditions are quite different. Specifically, it is found that the discrepancy between the intermittency of enstrophy and dissipation is reduced when small-scale motions become intense. In addition, the spatial distributions of intense enstrophy and dissipation are found to be correlated. Lastly, a quantitative relationship for enstrophy and dissipation is observed in these intense events. The similarity of enstrophy and dissipation in all of these aspects does not occur in low-Reynolds-number turbulence, and the current common findings could imply potential universality for intense small-scale turbulence. The conditional probability density functions of pressure Laplacian and velocity derivatives are also analyzed to further understand why dissipation and enstrophy become similar when small-scale motions become strong.

DOI: 10.1103/PhysRevFluids.5.014301

I. INTRODUCTION

Though the governing equations for the motion of incompressible viscous fluid have been established for nearly 200 years, the underlying mathematics and physics (namely, the turbulence phenomena) are still far from being comprehensively understood. A primary difficulty of this problem is the existence of a broad range of scales in fully turbulent flow. A widely accepted viewpoint about these scales is that the large-scale motions are flow specific, but the small scales are more likely to show universal characteristics [1,2]. Therefore, small-scale turbulence has been a optimal ground for developing a proper theory of turbulence. Apart from its theoretical significance, small-scale turbulence also plays an important role in many practical processes, such as the mixing of chemicals in reacting flow [3,4], quenching of flame in turbulent combustion [5], and preferential concentration of inertial particles in particulate flow [6].

Continuous efforts have been made to explore and understand the properties of small-scale turbulent motions [7–11]. A remarkable branch of this research is to discuss the spatial and statistical relations [12–17] between local enstrophy $\Omega = 2R_{ij}R_{ij}$ and the local dissipation rate $\varepsilon = 2\nu S_{ij}S_{ij}$ (the word "local" is omitted hereafter). Here, ν is the viscosity, and $S_{ij} = (\partial u_i/\partial x_j + \partial u_j/\partial x_i)/2$ and $R_{ij} = (\partial u_i/\partial x_j - \partial u_j/\partial x_i)/2$ are, respectively, the strain rate tensor and rotation rate tensor.

*fanjr@zju.edu.cn

However, conflicting results have been reported about this topic. Experimental measurement [18] and early numerical simulations [19,20] suggested that the same scaling exponents for dissipation and enstrophy may not be possible, and dissipation is typically less intermittent than enstrophy. Meanwhile, two analytical studies [21,22] pointed out that enstrophy and dissipation should have the same scaling exponent at sufficiently high Reynolds number, from the perspectives of statistical field theory [21] and vortex structures [22], respectively. They attributed the inconsistency of previous observations to finite Reynolds number. But evidence supporting their standpoint was scarce at that time.

However, the Reynolds number achieved in recent direct numerical simulations has grown quickly owing to the improvement of computing power [11,16,23,24]. Though it is still far from the typical Reynolds number in industrial and environmental applications, these high-fidelity simulations of box turbulence have brought new insights into the research of small-scale turbulence. It is reported that the extreme events of enstrophy and dissipation scale similarly as the Reynolds number increases [16,23], seemingly supporting the previous theoretical arguments [21,22]. Furthermore, it is found that intense dissipation and intense enstrophy tend to occur together in space at high Reynolds number [16,23,24].

Regarding the current knowledge about small-scale turbulence based on the above studies, there are two questions we would like to explore. First, in addition to the cases in Refs. [16,23], can we find other evidence supporting the conclusion that enstrophy and dissipation could be similar in certain conditions? Second, is a high Reynolds number the necessary and sufficient condition for this characteristic of small-scale turbulence? The questions originate from our recent research about turbulence modulation by finite-size particles [25]. In that work, it is found that the dissipation rate becomes quite intense due to the disturbance by particles, which is in agreement with other numerical [26] and experimental [27] studies. However, what is interesting is that several common results concerning the statistics of dissipation and enstrophy are observed with the single-phase high-Reynolds-number simulations.

This article is organized as follows. In Sec. II, the methodology and simulation configurations are introduced. In Sec. III A, the intermittency of enstrophy and dissipation are investigated. Their spatial distributions are then discussed in Sec. III B. To explain the similarity between enstrophy and dissipation, Sec. III C conducts analysis from the perspective of pressure Laplacian and velocity derivatives. Finally, Sec. IV gives a summary.

II. NUMERICAL METHODS AND SIMULATION CONFIGURATIONS

We consider the incompressible viscous flow laden with finite-size particles. The dimensionless form of the governing equations can be written as

$$\nabla \cdot \mathbf{u} = 0, \tag{1}$$

$$\frac{\partial \mathbf{u}}{\partial t} + \mathbf{u} \cdot \nabla \mathbf{u} = -\nabla p + \nu \nabla^2 \mathbf{u} + \mathbf{f}, \tag{2}$$

where $\mathbf{u}$ denotes the velocity vector, p is the kinematic pressure, and ν is the kinematic viscosity. The vector $\mathbf{f}$ is the volume force term representing the effects of particles on fluid. This force is determined in the framework of the immersed boundary technique. We solve Eqs. (1) and (2) using a sixth-order centered compact scheme [28] for the diffusion term, and the convective terms are discretized by a fifth-order upwind compact scheme [29]. The Poisson equations for pressure are solved by a fourth-order method [30]. The time integration of the equations is performed by the fourth-order Runge-Kutta scheme [31].

The no-slip and no-penetration boundary conditions at the fluid-solid interfaces are implemented by the direct-forcing immersed boundary method [32,33]. In this method, the surface of each particle is represented by a number of uniformly distributed Lagrangian points. The intermediate fluid velocity at the kth Lagrangian point $\mathbf{x}_k$, $\hat{\mathbf{u}}_k$ is then computed through the interpolation, in which

TABLE I. Parameters of the three particle-laden cases at the particle injection time. St means particle stokes number, which is defined by $\mathrm{St} = d_p^2\eta^2\rho_p/18\rho_f$, where ρ_p and ρ_f are the particle density and fluid density, respectively.

Case	ρ_p/ρ_f	d_p/η_{in}	$d_p/\lambda_{\mathrm{in}}$	St
P1	10.0	25.4	1.58	358.4
P2	100.0	25.4	1.58	3584.2
P3	1000.0	25.4	1.58	35842.2

the weights are determined by the Dirac δ function [34]. The direct forcing acting on the point $\mathbf{x}_k$ can be obtained as $\mathbf{F}_k(\mathbf{x}_k) = (\mathbf{u}_L - \hat{\mathbf{u}}_k)/\Delta t$, where Δt is the time step and $\hat{\mathbf{u}}_k$ is the desired velocity at position $\mathbf{x}_k$. The desired velocity means the fluid velocity at the next time level which satisfies the no-slip condition, which is given by $\mathbf{u}_L = \mathbf{u}_p + \boldsymbol{\omega}_p \times (\mathbf{x}_k - \mathbf{x}_c)$, where $\mathbf{u}_p$ is the translational velocity of particle, $\boldsymbol{\omega}_p$ is the rotational velocity of the particle, and $\mathbf{x}_c$ is the location of particle center. By iterating this scheme multiple times in one time step, the accuracy of the immersed boundary method can be further improved, as pointed out in Refs. [33,35]. The force term $\mathbf{f}$ thus can be integrated as $\mathbf{f} = \int_{\zeta_p} \mathbf{F}_k \cdot \delta(\mathbf{x} - \mathbf{x}_k) d\mathbf{x}_k$, where ζ_p is the particle domain and δ is the Dirac δ function. Accordingly, the hydrodynamic force $\mathbf{F}$ and torque $\mathbf{T}$ exerted on the particle are expressed as

$$\mathbf{F} = \rho_f \frac{d\mathbf{u}_p}{dt} V_p - \rho_f \int_1^N \mathbf{F}_k(\mathbf{x}_k) d\mathbf{x}_k, \tag{3}$$

$$\mathbf{T} = \frac{\rho_f}{\rho_p} I \frac{d\omega_p}{dt} - \rho_f \int_1^N (\mathbf{x}_k - \mathbf{x}_c)\mathbf{F}_k(\mathbf{x}_k) d\mathbf{x}_k, \tag{4}$$

where ρ_f and ρ_p are, respectively, the density of the fluid and particle. N is the total number of Lagrangian points on a particle, V_p is the volume of a particle, and I is the rotational inertia of the particles.

The particle-particle collisions have also been considered here. The soft-sphere collision model [36] is adopted to calculate the collision force and torque acting on the particles. The basic idea of the soft-sphere model is to represent the pair of colliding particles as a combination of spring, dashpot, and slider. Detailed implementations of the model are referred to Refs. [36,37]. It should be pointed out that the soft-sphere model is able to handle multiple collisions for a particle at a time. Once the hydrodynamic and collisional forces and torques are acquired, the particle velocity and location can be updated by marching forward the governing equations of particle motions, which are based on Newton's law. All of these methods have been validated in our previous works [33,35,37].

We perform direct numerical simulations of particle-laden isotropic turbulent flows at moderate Reynolds number. The dimensionless length of the box is 2π, and the computational domain is discretized into a uniform mesh with 1024^3 grid points. The initial Taylor-scale Reynolds number is $\mathrm{Re}_\lambda = 110$ and no turbulence forcing scheme is applied, namely, the flow is decaying. A total of 640 particles are randomly released in the fluid domain when the initial turbulent flow has developed sufficiently, which can be determined by whether the skewness of the velocity derivative reaches about 0.5. The diameter of particles, d_p, is 40 times the grid width, and 25.4 times the Kolmogorov length scale η at the particle injection time. The corresponding solid fraction is 2%. The dimensionless length of the Kolmogorov scale and Taylor scale at the injection time is, respectively, $\eta_{\mathrm{in}} = 9.66 \times 10^{-2}$ and $\lambda_{\mathrm{in}} = 1.55 \times 10^{-1}$. The Taylor-scale Reynolds number at particle release time is 66.5. To examine whether the discrepancy between enstrophy and dissipation decreases with the intensity of small-scale turbulence, three particle-laden simulations (cases P1–P3) are conducted with different particle-to-fluid density ratios, as shown in Table I. The initial states for the three cases are identical, but their mean particle slip velocities will soon differ from each other due to different

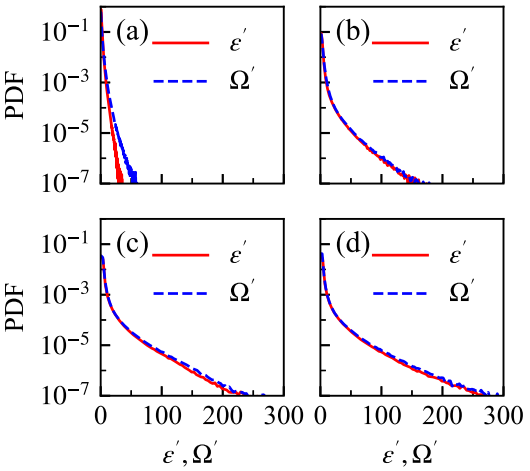

FIG. 1. PDFs of normalized dissipation rate and normalized enstrophy. Solid lines correspond to the normalized dissipation rate; dashed lines correspond to normalized enstrophy. (a)–(d) Cases SP, P1, P2, and P3, respectively.

particle inertias, and thus they can affect the small scales to different degrees. The corresponding single-phase flow is denoted as case SP to facilitate comparison.

III. RESULTS

In this section, the statistical and spatial relationships between enstrophy and dissipation are examined for both single-phase and particle-laden cases based on our simulations. Observations are compared with those single-phase but higher-Reynolds-number studies. The potential reason for those common features about small-scale turbulence, which occurred in flows with and without particles, is explored.

A. Intermittency of enstrophy and dissipation

The spatial intermittency of small-scale turbulence means that flow variables show extremely high local values relative to the spatial average. Following the definitions in Ref. [38], we call events with fluctuations over $O(10)$ times the mean as "extreme events." The intermittency for random variables could be intuitively characterized by their probability density functions (PDFs). Figure 1 shows the PDFs of normalized dissipation rate $\varepsilon' = \varepsilon/\langle\varepsilon\rangle$ and normalized enstrophy $\Omega' = \Omega/\langle\Omega\rangle$ at $t = 2.8\tau_0$, where τ_0 is the initial large-eddy turnover time, and the operator $\langle\cdot\rangle$ means spatial average over the fluid domain (excluding the regions occupied by particles). It should be pointed out that $\langle\varepsilon\rangle$ is equivalent to $\langle\Omega\rangle$ because $\langle\varepsilon\rangle = \nu\langle\Omega\rangle$ in homogeneous turbulence [39]. As can be seen from Fig. 1(a), it is evident that dissipation is less intermittent than enstrophy in single-phase turbulence at such Reynolds number, agreeing with the previous observations in single-phase turbulence [19,20]. For particle-laden flows at similar Reynolds number in Figs. 1(b)–1(d), both the intermittency of dissipation rate and that of enstrophy have been greatly augmented as a result of disturbance by particles. The higher the particle inertia is, the more intermittent the flow tends to be. In addition, the gaps between PDFs of enstrophy and dissipation are obviously narrowed.

Since the turbulence is decaying in the present simulations, it is necessary to examine whether the above observation stays the same when the Reynolds number changes. Figure 2 shows the temporal evolution of mean dissipation and mean enstrophy. At the particle injection time ($t = 0.8\tau_0$), the mean dissipation and mean enstrophy increase sharply, but after that the curves are rather smooth. In addition, the injection of particles does not lead to any derivations from the relation $\langle\varepsilon\rangle = \nu\langle\Omega\rangle$.

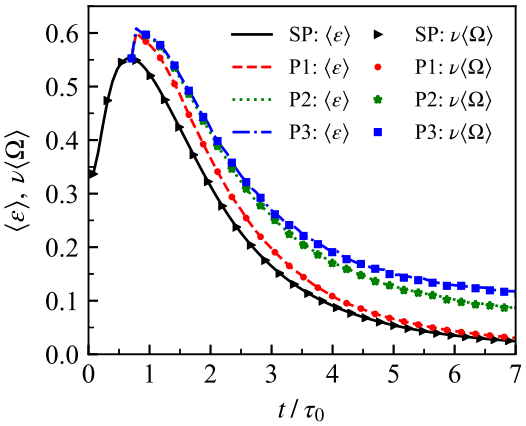

FIG. 2. Temporal evolution of the spatial mean values of dissipation rate (lines) and enstrophy (scatters).

That is to say, the mean values are not intermittent in time, though the local values are strongly intermittent in space. In Fig. 3, the PDFs of the normalized dissipation rate and enstrophy at several time snapshots are displayed for the single-phase case (SP) and the particle-laden case (P3) (the other two particle-laden cases are not shown here because the results are similar). The statistics in this work start from $t = 2.8\tau_0$ (two eddy turnover times after the injection) to get rid of the influence of initialization. From Fig. 3, it can be seen that the shapes of PDFs remain very similar as time goes by and the main conclusions keep the same: enstrophy is more intermittent than dissipation for single-phase turbulence at such low Reynolds number, but they are both greatly augmented in the particle-laden case and the gap between them is decreased.

In conclusion, the current results present the same behavior as the previous numerical [16,23,24] and theoretical [21,22] studies at high Reynolds number. Specifically, enstrophy becomes as intermittent as dissipation when the small-scale motions become intense.

Another problem concerning intermittency is whether high-order moments of dissipation and enstrophy converge. As the order of the moment increases, the contributions of intense values become more significant, though these events are rare in comparison to those with moderate

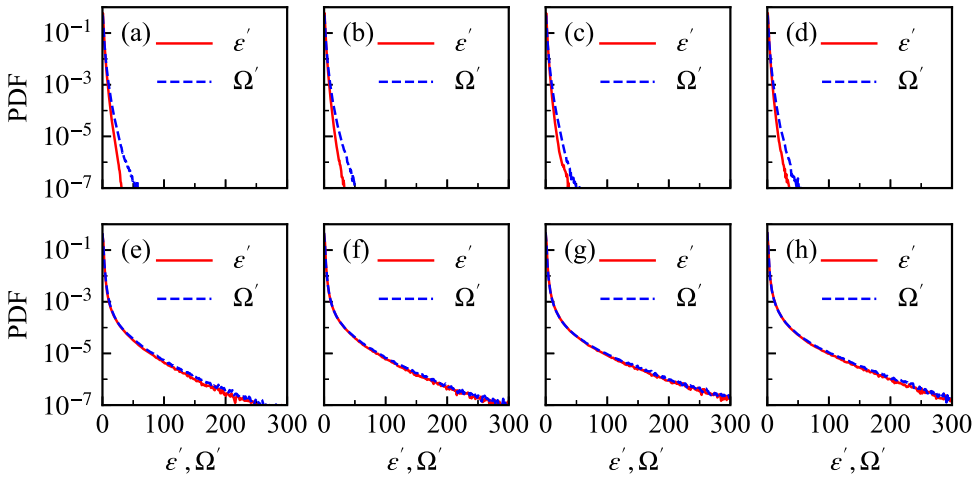

FIG. 3. PDFs of normalized dissipation and enstrophy for (a)–(d) the single-phase case (SP) and (e)–(h) the particle-laden case (P3) at different times. (a),(e) $2.8\tau_0$; (b),(f) $3.5\tau_0$; (c),(g) $4.2\tau_0$; (d),(h) $4.9\tau_0$.

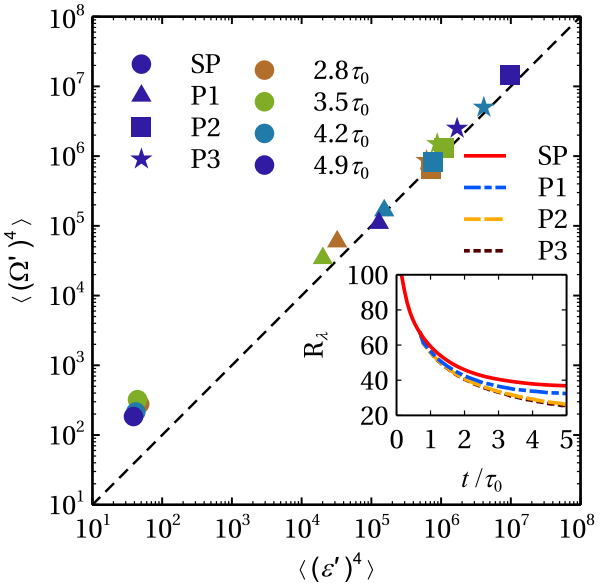

FIG. 4. Scatterplot of fourth-order moments of normalized dissipation and enstrophy. Each point stands for the spatial averages of enstrophy and dissipation at a time snapshot. Colors of the symbols indicate the time. Inset: The temporal development of Taylor-scale Reynolds number Re_λ.

values. If similar scaling of extreme values for dissipation and enstrophy is true, it is expected that the ratio of $\langle(\Omega')^p\rangle$ to $\langle(\varepsilon')^p\rangle$ decreases with Reynolds number and approaches unity when p is sufficiently large. The simulations in Ref. [23] suggest that $\langle(\Omega')^4\rangle/\langle(\varepsilon')^4\rangle$ generally decreases with Taylor-scale Reynolds number of the turbulence. Figure 4 shows the fourth-order moments of ε' and Ω' at different snapshots of the present simulations. Obviously, particles have greatly amplified both the moments of enstrophy and dissipation, with the maximum magnification up to $O(10^5)$ times within the snapshots. In general, heavy particles increase the moments more than light particles. It is reported in Ref. [23] that the ratio is closer to one for higher values of the moments, and there is a change in behavior at normalized moments around $O(10^5)$. In this work, $O(10^5)$ can also be roughly used as a pivot to separate the group of points.

Different from their observations, the similarity of dissipation and enstrophy does not occur at higher Reynolds number in this work. On the contrary, the two quantities are more close to each other in simulations with smaller Reynolds number. Table II displays the length scales and Reynolds number at the end of the simulations. It is found that the Reynolds number of the particle-laden case is smaller than that of the single-phase case. The reason could be due to smaller turbulence length scales. The particles generate small-scale turbulence, thus the turbulence length scales are smaller than those without particles, as shown in Table II. What the two kinds of flows (single-phase

TABLE II. Taylor-scale Reynolds number Re_λ, Taylor length scale λ (dimensionless) and Kolmogorov length scale η (dimensionless) at $t = 4.9\tau_0$.

Case	Re_λ	λ	η	η/η_{in}
SP	36.3	2.51×10^{-1}	2.12×10^{-2}	2.19
P1	30.5	2.17×10^{-1}	2.00×10^{-2}	2.07
P2	21.7	1.41×10^{-1}	1.53×10^{-2}	1.59
P3	21.3	1.29×10^{-1}	1.43×10^{-2}	1.48

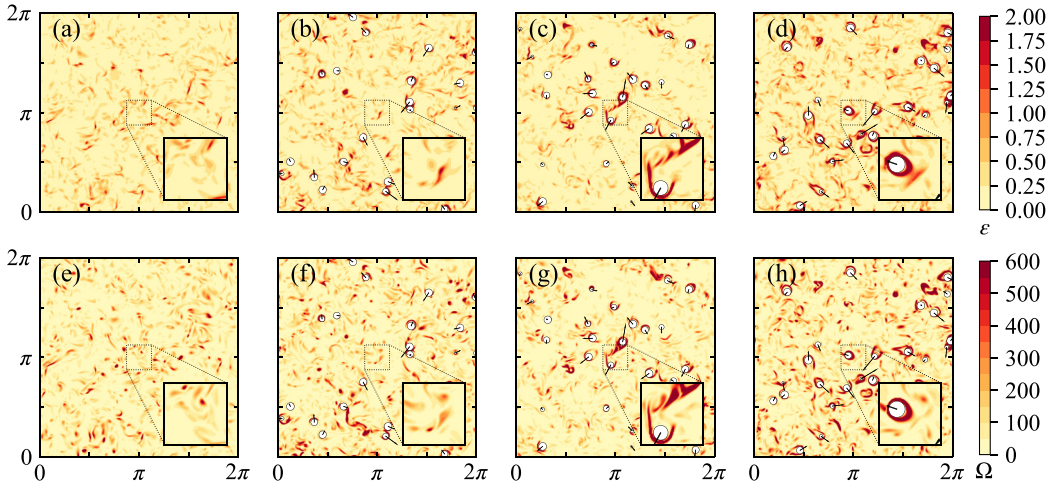

FIG. 5. Contour plots of local dissipation and enstrophy (both dimensionless). (a)–(d) The 2D slice views of dissipation; (e)–(h) views of enstrophy. Contours for cases SP, P1, P2, and P3 are displayed on different columns, respectively.

high-Reynolds number flow and particle-laden flow at low Reynolds number) have in common is that the small-scale motions are rather intense. It seems that not the high Reynolds number, but the intensity of the small scales is the key factor for this particular feature of similarity.

B. Spatial distributions of intense enstrophy and dissipation

Another recently observed characteristic of intense small-scale turbulence is that high dissipation and high enstrophy occur simultaneously in space, which was reported by the high-Reynolds-number simulations [23,24] and experiments [40]. Figure 5 shows the contours of local dissipation and enstrophy for different cases at the same time and cut plane. For case SP, the distribution of strong dissipation does not apparently coincide with that of strong enstrophy, as shown in Figs. 5(a) and 5(e). However, in the particle-laden cases, maps of intense enstrophy and dissipation induced by finite-size particles are overall matched. The current finding might be an evidence supporting this potential feature of intense small-scale turbulence.

To further quantitatively investigate whether the distributions of intense dissipation and intense enstrophy converge in space, we plot the joint PDFs of ε' and Ω', as displayed in Fig. 6. The contours in the first quadrants represent flow regions with both high enstrophy and high dissipation, and so forth. In Fig. 6(a), these two quantities do not show much correlation in the first quadrant. Meanwhile, in the high-Reynolds-number simulations by Yeung *et al.* [23], they observed a small protuberance along the diagonal line in the first quadrant at $\mathrm{Re}_\lambda = 1000$, suggesting the trend that intense dissipation and intense enstrophy occur together. For the particle-laden cases in Figs. 6(b)–6(d), the shapes of PDFs in the second, third, and fourth quadrants look similar to that of the single-phase flow. However, they are quite different in the first quadrants. It can be seen distinctly from the figure that intense dissipation is strongly correlated with intense enstrophy. This is another common observation with single-phase high-Reynolds-number studies. The correlation is even more obvious than that in Ref. [23], though the Taylor-scale Reynolds number is one order smaller in the present simulations. They look more like thorns rather than small protuberances at the top right corner of the contours. More importantly, the trend of these sharp corners in the direction of increasing dissipation and enstrophy is exactly in accord with the auxiliary diagonal lines (gray dashed lines with slope of one) in all the particle-laden cases. It is suggested that not only are intense enstrophy and intense dissipation associated with each other in space, but

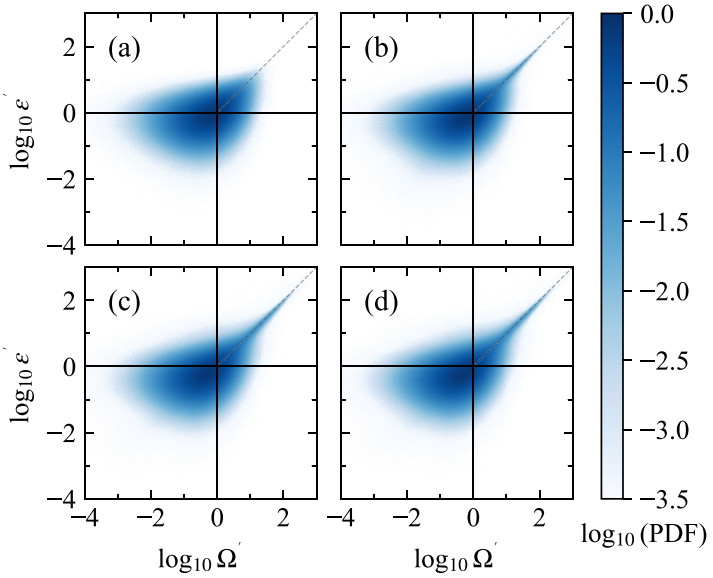

FIG. 6. Joint PDFs of normalized dissipation rate and normalized enstrophy. (a) Case SP, (b) case P1, (c) case P2, and (d) case P3. The slope of the gray dashed lines in the first quadrants is 1.

also there exists a quantitative relationship between their instantaneous local values. As can be inferred from Figs. 6(b)–6(d), this quantitative relationship is that ε'/Ω' tends to be 1 for intense small-scale turbulence. Analogue to Fig. 3, Fig. 7 displays the joint PDFs of normalized dissipation and normalized enstrophy for the single-phase case (SP) and the particle-laden case (P3) at different times. It can be seen that the joint PDFs look much the same as time changes, indicating that the statistics are not intermittent in time.

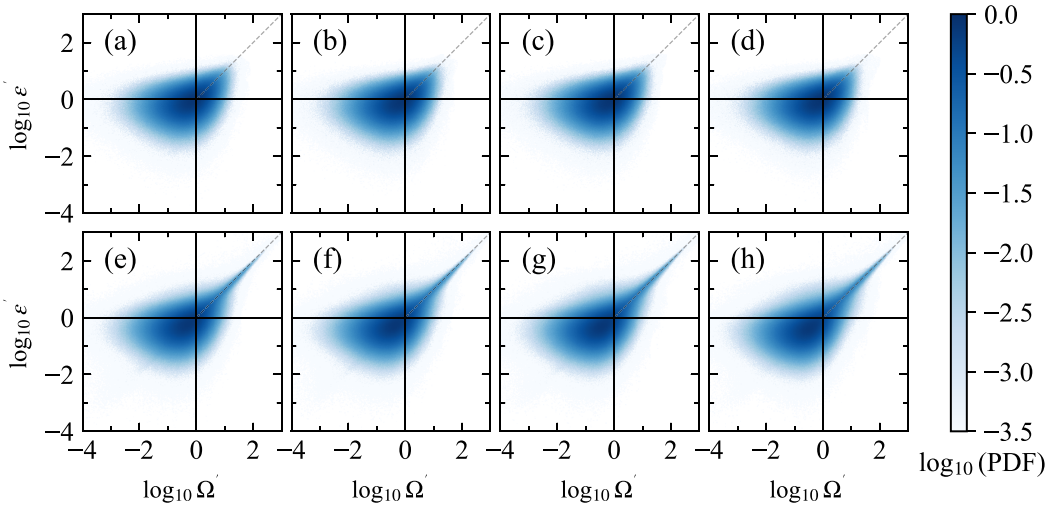

FIG. 7. Joint PDFs of normalized dissipation and normalized enstrophy for (a)–(d) the single-phase case (SP) and (e)–(h) the particle-laden case (P3) at different times. (a),(e) $2.8\tau_0$; (b),(f) $3.5\tau_0$; (c),(g) $4.2\tau_0$; (d),(h) $4.9\tau_0$.

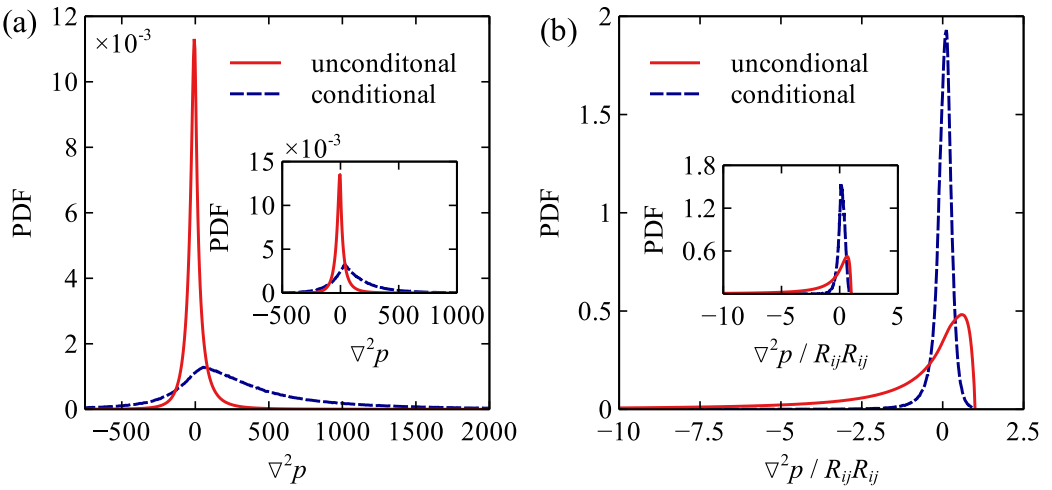

FIG. 8. Comparison of PDFs conditioned on intense events ($\varepsilon' \geqslant 10$ and $\Omega' \geqslant 10$) and on full domain (unconditional) for case P3. (a) PDFs of $\nabla^2 p$; (b) PDFs of $\nabla^2 p/R_{ij}R_{ij}$. Insets: The corresponding PDFs for the single-phase case (SP).

C. Reasons for the similarity between enstrophy and dissipation

As mentioned above, $\langle\varepsilon\rangle$ is equivalent to $\langle\Omega\rangle$ in homogeneous turbulence, and Fig. 2 has proved that particles do not cause biases from the equality. Therefore, one can simplify the ratio of ε' to Ω' as $R_{ij}R_{ij}/S_{ij}S_{ij}$. In the turbulence literature, the difference of the square of rotation rate tensor R_{ij} and that of strain rate tensor S_{ij} is usually used to identify the vortex structures, which is known as the Q criterion [41] and $Q = (R_{ij}R_{ij} - S_{ij}S_{ij})/2$. Substituting the expressions of strain rate and rotation rate into the square terms, we can write the difference of $R_{ij}R_{ij}$ and $S_{ij}S_{ij}$ in forms of velocity derivatives as

$$R_{ij}R_{ij} - S_{ij}S_{ij} = -\frac{\partial u_i}{\partial x_j}\frac{\partial u_j}{\partial x_i}. \tag{5}$$

Utilizing the continuity equation and momentum equation for incompressible flow, Eq. (5) can be associated with the pressure Laplacian by

$$\nabla^2 p = -\frac{\partial u_i}{\partial x_j}\frac{\partial u_j}{\partial x_i}. \tag{6}$$

These two equations offer us the opportunity to gain a greater understanding of the intense events of enstrophy and dissipation from the perspectives of pressure Laplacian and velocity derivatives.

Since the pressure Laplacian are closely related to dissipation and enstrophy by $R_{ij}R_{ij} - S_{ij}S_{ij} = \nabla^2 p$, we are very interested in the behavior of the pressure Laplacian when enstrophy and dissipation become similar. It should be pointed out that "become similar" means $S_{ij}S_{ij}/R_{ij}R_{ij} = 1$ when small-scale motions are intense. It is known that when small-scale motions get intense, both $R_{ij}R_{ij}$ and $S_{ij}S_{ij}$ become large, so how about $\nabla^2 p$? One possible situation may be $\nabla^2 p = 0$ so that $S_{ij}S_{ij}/R_{ij}R_{ij} = 1$ is ensured. Another situation is that the absolute value of $\nabla^2 p$ also becomes large, but $\nabla^2 p/R_{ij}R_{ij} = 0$, so $S_{ij}S_{ij}/R_{ij}R_{ij} = 1$ is still satisfied according to $1 - S_{ij}S_{ij}/R_{ij}R_{ij} = \nabla^2 p/R_{ij}R_{ij}$.

To answer this question, we consider the PDFs of $\nabla^2 p$ conditioned on $\varepsilon' \geqslant 10$ and $\Omega' \geqslant 10$ following the definition in Ref. [38]. Figure 8(a) compares the conditional PDFs and unconditional PDFs (namely, PDFs on full domain) of $\nabla^2 p$ for case P3 and case SP (inset). It can be found that the unconditional PDFs have sharp shapes, which suggests that there is a high possibility for $\nabla^2 p$ being zero, but low chance for $|\nabla^2 p|$ being large. Besides, the unconditional PDFs are symmetric,

so the chances for $\nabla^2 p$ being positive and negative are in balance. The distribution patterns for conditional PDFs are far different. First, the conditional PDFs have significantly larger variance and they look much shorter than the unconditional PDFs. Although the maximum probability still occurs at around $\nabla^2 p = 0$, the chance for high $|\nabla^2 p|$ has increased and the curves have gentler slopes. Second, the conditional PDFs are no longer symmetric and positively skewed. The most important conclusion obtained from Fig. 8(a) is that the conjecture that $\nabla^2 p = 0$ for intense events is not true. The possibility of pressure Laplacian being large and positive is increased when conditioned on high enstrophy and high dissipation zones.

Then the only potential situation should be that though $\nabla^2 p$ has a higher value as the intensity of small scales increases, $\nabla^2 p/R_{ij}R_{ij}$ or $\nabla^2 p/S_{ij}S_{ij}$ becomes negligible in such condition. This inference is obtained according to $1 - S_{ij}S_{ij}/R_{ij}R_{ij} = \nabla^2 p/R_{ij}R_{ij}$ or $R_{ij}R_{ij}/S_{ij}S_{ij} - 1 = \nabla^2 p/S_{ij}S_{ij}$. Without loss of generality, we examine the conditional PDFs of $\nabla^2 p/R_{ij}R_{ij}$, which are shown in Fig. 8(b). As expected, the peaks of the PDFs of $\nabla^2 p/R_{ij}R_{ij}$ are shifted towards zero when conditioned on extreme events, and the conditional PDFs have much smaller variance compared to the unconditional PDFs. In addition, unconditional PDFs are nonsymmetric with very long tails on the negative side, and they have higher amplitude on the positive side. By contrast, the conditional PDFs are more likely to be symmetric, and the tails on the negative side have been greatly shortened, indicating a low chance for $\nabla^2 p/R_{ij}R_{ij}$ being both large and negative in extreme events. The physical interpretation of small $\nabla^2 p/R_{ij}R_{ij}$ for intense small-scale turbulence could then be that as the velocity fluctuations grow, the magnitude of the corresponding pressure fluctuation does not seem to increase equally.

Though we could explain why $R_{ij}R_{ij}$ gets close to $S_{ij}S_{ij}$ from the aspect of pressure Laplacian, it is still unclear why $\nabla^2 p$ is much smaller in comparison to $R_{ij}R_{ij}$. For this reason, we would like to explore the internal cause from the viewpoint of velocity derivatives themselves. Expanding $\nabla^2 p$ and $R_{ij}R_{ij}$ following the Einstein summation convention, one can get $\nabla^2 p = -(A + 2B)$ and $R_{ij}R_{ij} = C - B$, where

$$A = \left(\frac{\partial u_1}{\partial x_1}\right)^2 + \left(\frac{\partial u_2}{\partial x_2}\right)^2 + \left(\frac{\partial u_3}{\partial x_3}\right)^2, \tag{7}$$

$$B = \frac{\partial u_1}{\partial x_2}\frac{\partial u_2}{\partial x_1} + \frac{\partial u_1}{\partial x_3}\frac{\partial u_3}{\partial x_1} + \frac{\partial u_2}{\partial x_3}\frac{\partial u_3}{\partial x_2}, \tag{8}$$

$$C = \frac{1}{2}\left[\left(\frac{\partial u_1}{\partial x_1}\right)^2 + \left(\frac{\partial u_2}{\partial x_1}\right)^2 + \left(\frac{\partial u_1}{\partial x_3}\right)^2 + \left(\frac{\partial u_3}{\partial x_1}\right)^2 + \left(\frac{\partial u_2}{\partial x_3}\right)^2 + \left(\frac{\partial u_3}{\partial x_2}\right)^2\right]. \tag{9}$$

The terms on the right-hand sides of Eqs. (7)–(9) can be roughly divided into two categories: the square terms and the cross terms of two different velocity derivatives. There may be changes in the behavior of the terms consisting of them, which leads to the changes in the behavior of enstrophy and dissipation for intense small-scale turbulence. For the square terms, it is relatively clear that they become larger when the intensity of small-scale turbulence increases, but we have no idea about the cross terms.

Figure 9(a) shows the joint PDF of $\partial u_1/\partial x_2$ and $\partial u_2/\partial x_1$ for case P3. The contours are symmetric to the two axes when the magnitudes of the derivatives are relatively low. Namely, the points in this plane have an equal chance to fall in the four quadrants when they are not far from the origin. However, situations are different for intense events. The points are more likely to fall in the second and fourth quadrants when the magnitudes of the derivatives are large. This preferential distribution makes the shape of the PDF asymmetric, and they spread out along the diagonal line with slope of -1. It is obvious in Fig. 9(a) that the contour looks much blanker in the first and third quadrants in comparison to the second and fourth quadrants. Mathematically speaking, it is implied that the product of the two terms is more likely to be negative in intense events. Then a reasonable inference is that each of the cross product terms in B tends to be negative when conditioned on high enstrophy and high dissipation zones. Therefore, the term B should also tend to be negative in this condition.

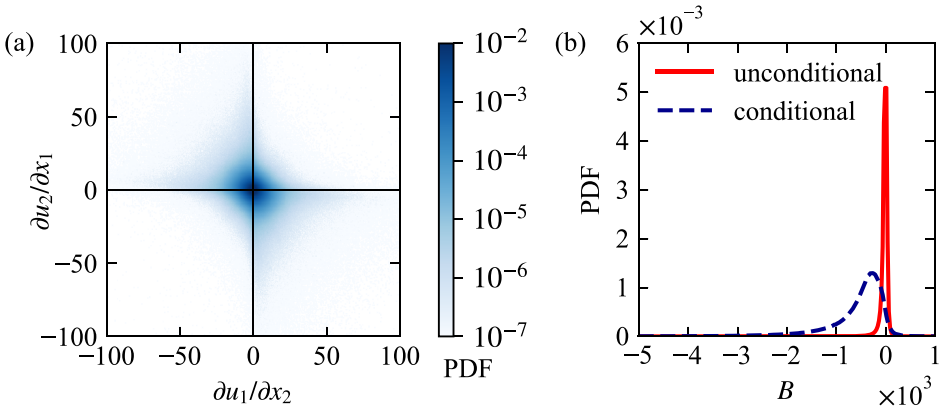

FIG. 9. PDFs of the velocity derivatives for case P3. (a) Joint PDF of $\partial u_1/\partial x_2$ and $\partial u_2/\partial x_1$. (b) Unconditional and conditional PDFs of term B.

Figure 9(b) shows the comparisons of unconditional and conditional PDFs of B. For unconditional PDF, it takes some effort to see that it has a slightly longer tail in the negative side than in the positive side. By contrast, it can be seen more clearly that the conditional PDF mainly lies in the negative side, which demonstrates the above conclusion. In addition, the conditional PDFs have long stretched tails in the negative side, indicating that the absolute value of B becomes larger when conditioned on intense events.

But could this particular property of term B explain why $\nabla^2 p/R_{ij}R_{ij}$ tends to be small and thereby why $S_{ij}S_{ij}$ approaches $R_{ij}R_{ij}$? The absolute values of A, B, and C should all increase when they are conditioned on intense events. However, A and C always keep positive, but B preferentially becomes negative in intense small-scale turbulence. As a result, $\nabla^2 p = -(A + 2B)$ can be considered as the summation of two opposite contributions which cancel each other out, while $R_{ij}R_{ij} = C - B$ consists of two positive parts. This could be a rough explanation for why $\nabla^2 p$ is much smaller than $R_{ij}R_{ij}$ in intense events.

IV. CONCLUSIONS

In the present study, we propose an idea to explore the properties of small-scale turbulence in particle-laden turbulent flow. It is found that the finite-size particles greatly increase the small-scale turbulence. In this particle-enhanced turbulent flow, similar features (both statistical and spatial) between enstrophy and dissipation are observed. These findings support the previous theoretical inferences. In addition, a quantitative relation between intense dissipation and enstrophy is found. The statistics of pressure Laplacian and velocity derivatives are conducted to look for clues about why enstrophy and dissipation become similar. It turns out that the cross product of the velocity derivatives is negative in intense small-scale turbulence which leads to the similarity of enstrophy and dissipation.

It is interesting that there are common observations between this particle-enhanced turbulence and the recent single-phase high-Reynolds-number turbulence. Though the Reynolds number is quite different (more than one order of magnitude), the common characteristic is that the small-scale motions are rather intense, which could be the key factor for these behaviors.

ACKNOWLEDGMENTS

The authors are grateful for the support of this research by the National Natural Science Foundation of China (Grant No. 51836007) as well as the National Program for Support of Top-notch Young Professionals.

[1] M. Nelkin, Universality and scaling in fully developed turbulence, Adv. Phys. **43**, 143 (1994).
[2] K. R. Sreenivasan and R. A. Antonia, The phenomenology of small-scale turbulence, Annu. Rev. Fluid Mech. **29**, 435 (1997).
[3] J. M. Ottino, Mixing, chaotic advection, and turbulence, Annu. Rev. Fluid Mech. **22**, 207 (1990).
[4] P. E. Dimotakis, Turbulent mixing, Annu. Rev. Fluid Mech. **37**, 329 (2005).
[5] N. Peters, Local quenching due to flame stretch and non-premixed turbulent combustion, Combust. Sci. Technol. **30**, 1 (1983).
[6] K. D. Squires and J. K. Eaton, Preferential concentration of particles by turbulence, Phys. Fluids A **3**, 1169 (1991).
[7] A. N. Kolmogorov, The local structure of turbulence in incompressible viscous fluid for very large Reynolds numbers, Dokl. Akad. Nauk SSSR **30**, 299 (1941).
[8] A. N. Kolmogorov, A refinement of previous hypotheses concerning the local structure of turbulence in a viscous incompressible fluid at high Reynolds number, J. Fluid Mech. **13**, 82 (1962).
[9] G. Elsinga and I. Marusic, Universal aspects of small-scale motions in turbulence, J. Fluid Mech. **662**, 514 (2010).
[10] E. D. Siggia, Numerical study of small-scale intermittency in three-dimensional turbulence, J. Fluid Mech. **107**, 375 (1981).
[11] T. Ishihara, Y. Kaneda, M. Yokokawa, K. Itakura, and A. Uno, Small-scale statistics in high-resolution direct numerical simulation of turbulence: Reynolds number dependence of one-point velocity gradient statistics, J. Fluid Mech. **592**, 335 (2007).
[12] J. M. Burgers, A mathematical model illustrating the theory of turbulence, in *Advances in Applied Mechanics* (Elsevier, New York, 1948), Vol. 1, pp. 171–199.
[13] R. Betchov, An inequality concerning the production of vorticity in isotropic turbulence, J. Fluid Mech. **1**, 497 (1956).
[14] W. T. Ashurst, A. Kerstein, R. Kerr, and C. Gibson, Alignment of vorticity and scalar gradient with strain rate in simulated navier–stokes turbulence, Phys. Fluids **30**, 2343 (1987).
[15] J. Schumacher, B. Eckhardt, and C. R. Doering, Extreme vorticity growth in Navier-Stokes turbulence, Phys. Lett. A **374**, 861 (2010).
[16] D. Donzis, P. Yeung, and K. Sreenivasan, Dissipation and enstrophy in isotropic turbulence: Resolution effects and scaling in direct numerical simulations, Phys. Fluids **20**, 045108 (2008).
[17] R. Kerr, Dissipation and enstrophy statistics in turbulence: Are the simulations and mathematics converging? J. Fluid Mech. **700**, 1 (2012).
[18] B. W. Zeff, D. D. Lanterman, R. McAllister, R. Roy, E. J. Kostelich, and D. P. Lathrop, Measuring intense rotation and dissipation in turbulent flows, Nature (London) **421**, 146 (2003).
[19] R. M. Kerr, Higher-order derivative correlations and the alignment of small-scale structures in isotropic numerical turbulence, J. Fluid Mech. **153**, 31 (1985).
[20] S. Chen, K. R. Sreenivasan, and M. Nelkin, Inertial Range Scalings of Dissipation and Enstrophy in Isotropic Turbulence, Phys. Rev. Lett. **79**, 1253 (1997).
[21] M. Nelkin, Enstrophy and dissipation must have the same scaling exponent in the high reynolds number limit of fluid turbulence, Phys. Fluids **11**, 2202 (1999).
[22] G. He, S. Chen, R. H. Kraichnan, R. Zhang, and Y. Zhou, Statistics of Dissipation and Enstrophy Induced by Localized Vortices, Phys. Rev. Lett. **81**, 4636 (1998).
[23] P. Yeung, D. Donzis, and K. Sreenivasan, Dissipation, enstrophy and pressure statistics in turbulence simulations at high reynolds numbers, J. Fluid Mech. **700**, 5 (2012).
[24] P. Yeung, X. Zhai, and K. R. Sreenivasan, Extreme events in computational turbulence, Proc. Nat. Acad. Sci. USA **112**, 12633 (2015).
[25] K. Luo, Z. Wang, D. Li, J. Tan, and J. Fan, Fully resolved simulations of turbulence modulation by high-inertia particles in an isotropic turbulent flow, Phys. Fluids **29**, 113301 (2017).
[26] F. Lucci, A. Ferrante, and S. Elghobashi, Modulation of isotropic turbulence by particles of taylor length-scale size, J. Fluid Mech. **650**, 5 (2010).
[27] T. Tanaka and J. K. Eaton, Sub-Kolmogorov resolution particle image velocimetry measurements of particle-laden forced turbulence, J. Fluid Mech. **643**, 177 (2010).

[28] C. A. Kennedy and M. H. Carpenter, Comparison of several numerical methods for simulation of compressible shear layers, NASA Technical Reports, Report No. 19980004143, 1997 (unpublished).
[29] M. M. Rai and P. Moin, Direct simulations of turbulent flow using finite-difference schemes, J. Comput. Phys. **96**, 15 (1991).
[30] U. Ananthakrishnaiah, R. Manohar, and J. W. Stephenson, Fourth-order finite difference methods for three-dimensional general linear elliptic problems with variable coefficients, Numer. Methods Parts D and E **3**, 229 (1987).
[31] A. Jameson and W. Schmidt, Some recent developments in numerical methods for transonic flows, Comput. Methods Appl. Mech. Eng. **51**, 467 (1985).
[32] M. Uhlmann, An immersed boundary method with direct forcing for the simulation of particulate flows, J. Comput. Phys. **209**, 448 (2005).
[33] K. Luo, Z. Wang, J. Fan, and K. Cen, Full-scale solutions to particle-laden flows: Multidirect forcing and immersed boundary method, Phys. Rev. E **76**, 066709 (2007).
[34] B. E. Griffith and C. S. Peskin, On the order of accuracy of the immersed boundary method: Higher order convergence rates for sufficiently smooth problems, J. Comput. Phys. **208**, 75 (2005).
[35] Z. Wang, J. Fan, and K. Luo, Combined multi-direct forcing and immersed boundary method for simulating flows with moving particles, Int. J. Multiphase Flow **34**, 283 (2008).
[36] P. A. Cundall and O. D. Strack, A discrete numerical model for granular assemblies, Geotech. J. **29**, 47 (1979).
[37] K. Luo, J. Tan, Z. Wang, and J. Fan, Particle-resolved direct numerical simulation of gas-solid dynamics in experimental fluidized beds, AlChE J. **62**, 1917 (2016).
[38] D. A. Donzis and K. Sreenivasan, Short-term forecasts and scaling of intense events in turbulence, J. Fluid Mech. **647**, 13 (2010).
[39] P. Davidson, *Turbulence: An Introduction for Scientists and Engineers* (Oxford University Press, New York, 2015).
[40] E.-W. Saw, D. Kuzzay, D. Faranda, A. Guittonneau, F. Daviaud, C. Wiertel-Gasquet, V. Padilla, and B. Dubrulle, Experimental characterization of extreme events of inertial dissipation in a turbulent swirling flow, Nat. Commun. **7**, 12466 (2016).
[41] J. C. R. Hunt, A. A. Wray, and P. Moin, Eddies, streams, and convergence zones in turbulent flows, in *Proceedings of the Summer Program* (Center for Turbulence Research, 1988), pp. 193–208.